

# Discontinuous transtensional rupture during the Mw 7.2 1995 Gulf of Aqaba earthquake

Hannes Vasyura-Bathke  \*<sup>1,2,3</sup>, Andreas Steinberg <sup>4</sup>, Frank Krüger<sup>2</sup>, Guangcai Feng<sup>5</sup>, P. Martin Mai <sup>1</sup>, Sigurjón Jónsson <sup>1</sup>

<sup>1</sup>King Abdullah University of Science and Technology (KAUST), Thuwal 23955-6900, Saudi Arabia, <sup>2</sup>University of Potsdam, D-14476 Potsdam, Germany, <sup>3</sup>Now at: Helmholtz Centre Potsdam, German Research Centre for Geosciences GFZ, <sup>4</sup>BGR, Federal Institute for Geosciences and Natural Resources, D-30655 Hannover, Germany, <sup>5</sup>Central South University, Changsha, China

**Author contributions:** *Conceptualization:* H. Vasyura-Bathke, S. Jónsson. *Methodology:* H. Vasyura-Bathke, A. Steinberg. *Software:* H. Vasyura-Bathke, A. Steinberg. *Formal Analysis:* H. Vasyura-Bathke, A. Steinberg, G. Feng. *Writing - original draft:* H. Vasyura-Bathke, A. Steinberg. *Writing - Review & Editing:* H. Vasyura-Bathke, A. Steinberg, F. Krüger, P. M. Mai, S. Jónsson, G. Feng. *Visualization:* H. Vasyura-Bathke. *Supervision:* F. Krüger, P. M. Mai, S. Jónsson. *Funding acquisition:* S. Jónsson.

**Abstract** The Gulf of Aqaba earthquake occurred on 22 November 1995 in the Northern Red Sea and is the largest instrumentally recorded earthquake in the region to date. The event was extensively studied during the initial years following its occurrence. However, it remained unclear which of the many faults in the gulf were activated during the earthquake. We present results from multi-array back projection that we use to inform Bayesian kinematic rupture models constrained by geodetic and teleseismic data. Our results indicate that most of the moment release was on the Aragonese fault via left-lateral strike slip and shallow normal faulting that may have been dynamically triggered by an early rupture phase on the Arnona fault. We also identified a predominantly normal-fault segment on the eastern shore of the gulf that was activated in the event. We dismiss the previously proposed hypothesis of a co-seismic sub-event on the western shore of the gulf and confirm that observed deformation can be rather attributed to post-seismic activity. In conclusion, the gulf shows many signs of active tectonic extension. Therefore, more events close to the shorelines are to be expected in the future and should be considered when conducting infrastructure projects in the region.

**Non-technical summary** The 1995 Gulf of Aqaba earthquake was a significant event that has been reexamined using a modern, multifaceted approach. By combining space geodetic satellite data and seismic waveform data, we have gained a more complete understanding of the earthquake, while taking into account potential errors in our analysis. Our results show that during the 1995 earthquake, three faults were activated across distinct fault segments: the Arnona fault in the south, the adjacent Aragonese fault in the north, and an undisclosed fault on the eastern shore of the gulf. These faults exhibited predominantly horizontal motion but also revealed a significant vertical component, underscoring the extension of the gulf. This discovery holds profound implications, particularly given the considerable infrastructure projects currently underway in the Gulf of Aqaba, i.e. within NEOM. In light of these developments, it is evident that earthquake modeling in the region is of paramount importance. The findings from this study underscore the necessity for updated hazard assessments and the establishment of plausible scenarios for potential future earthquakes.

Production Editor:  
Gareth Funning  
Handling Editor:  
Mathilde Radiguet  
Copy & Layout Editor:  
Théa Ragon

Received:  
October 20, 2023  
Accepted:  
February 2, 2024  
Published:  
February 19, 2024

## 1 Introduction

The Gulf of Aqaba is located at the southern end of the Dead Sea fault, which is a left-lateral transform fault system with an estimated average slip rate of  $\sim 5 \pm 1$  mm/yr during the Holocene (Le Béon et al., 2012; Lefevre et al., 2018). Geodetic observations show that the current left-lateral interseismic motion in the gulf is similar to that of the Dead Sea fault, with a small amount of opening across the gulf (ArRajehi et al., 2010; Li et al., 2021; Castro-Perdomo et al., 2022; Viltres et al., 2022). This transtensional motion has resulted in a complex tectonic setting of several transform faults and pull-apart basins within the 180-km-long Gulf of Aqaba (Ben-Avraham, 1985; Ribot et al., 2021, Fig.1). The area has

also been the seismically most active part of the Dead Sea transform fault with persistent micro-earthquake activity, several seismic swarms, and major events in the past several decades (e.g., Klinger et al., 1999).

The 22 November 1995 (gCMT time 04:15:26.2) Gulf of Aqaba earthquake (Mw 7.2) is the largest instrumentally recorded event in the northern Red Sea and along the entire 1000-km-long Dead Sea transform fault system (Fig. 1). Multiple studies on the earthquake have been published with both point and finite-fault models estimated, either from seismic data (Pinar and Türkelli, 1997; Klinger et al., 1999; Hofstetter et al., 2003) or geodetic data (Klinger et al., 2000; Baer et al., 2001; Shamir et al., 2003; Baer et al., 2008, Supplement Tab. S2, Fig.1). Due to the use of different datasets and the complex tectonic setting, the derived models are diverse and have high epistemic uncertainty, to the point

\*Corresponding author: vasbath@gfz-potsdam.de

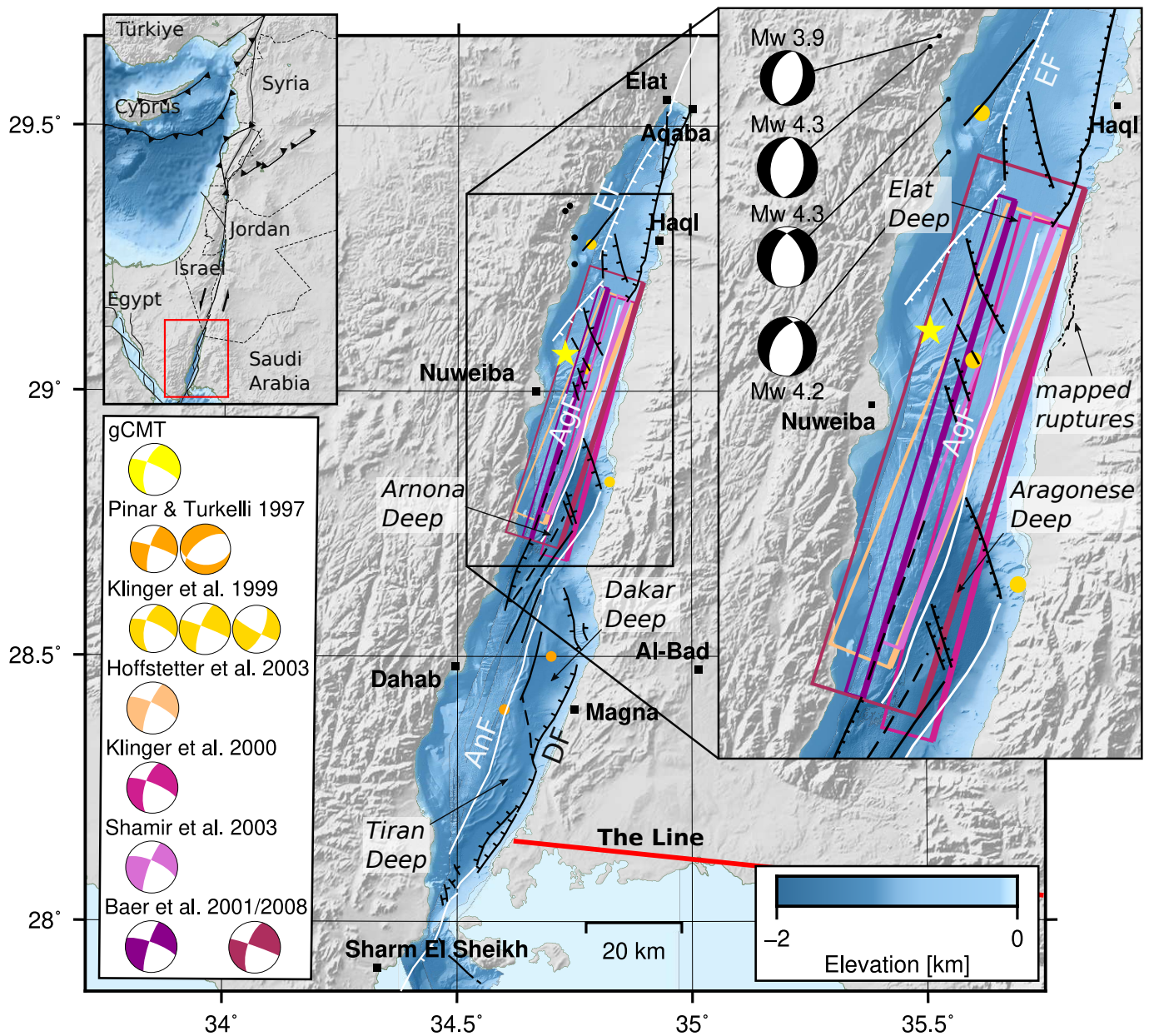


**Figure 1** Map of the Gulf of Aqaba and previously estimated finite and point source solutions (from the list compiled in Supplement Tab. S2). The Gulf of Aqaba consists of three pull-apart basins from North to South; the Elat Deep, the Aragonese Deep and the Dakar-Tiran Deep bounded by three main strike-slip faults (white) and normal faults (black) (Ribot et al., 2021). Focal mechanisms of the 1995 event (sizes scaled by magnitude, Supplement Tab. S2) are color coded by the respective location of estimated point (dots) or finite sources (rectangles) in the maps. The upper right inset shows a zoom-in to the epicentral region, where on-land normal faulting (black) attributed to the 1995 event was mapped on the East coast of the Gulf (Lefevre, 2018). The four black focal mechanisms are selected aftershocks to the Gulf of Aqaba earthquake potentially contributing to post-seismic deformation (Hofstetter et al., 2003; Baer et al., 2008). Shaded topography is from SRTM3 (Farr et al., 2007) and bathymetry data is from (Ribot et al., 2021). AgF- Aragonese Fault, AnF- Arnona Fault, EF- Elat Fault, DF- Dakar Fault. The yellow star shows the epicentre of the Gulf of Aqaba earthquake as determined by gCMT. The upper left inset shows the region of interest (red) at the southern Dead Sea transform fault system (modified from Castro-Perdomo et al. (2022)).

that there is no clear consensus on the rupture process of the earthquake. Nonetheless, most of the studies found that the majority of the seismic moment was released on the Aragonese Fault (AgF) in the central part of the gulf (Fig. 1). However, visible complexities in teleseismic broadband waveforms and in surface-displacement maps derived from interferometric synthetic aperture radar (InSAR) suggest a more complex multi-fault rupture in the gulf. Based on the teleseismic waveform data complexity, different number of sub-events and candidates of potentially activated faults have been proposed, which involve the Elat Fault (EF), the Arnona Fault (AnF) and the Dakar Fault (DF), as well as the Aragonese Fault (Pinar and Türkelli, 1997; Klinger et al., 1999; Shamir et al., 2003).

The sparsity of available near-field geodetic data and far-field seismic data makes it difficult to study the details of the earthquake rupture process. The main fault rupture was off-shore within the gulf and InSAR data are, therefore, not available in the near-field of the earthquake (Klinger et al., 2000; Baer et al., 2001, 2008). Also, the roughly N-S striking orientations of the involved faults limit the capability of obtaining the full surface displacement field with InSAR, as radar line-of-sight (LOS) observations are not very sensitive to the predominant North-South coseismic surface displacements. Furthermore, SAR-image acquisitions were infrequent and irregular in this region in the 1990s (Supplement Tab. S1). Finally, notable post-seismic activity, particularly aftershocks, were reported on the Egyptian side of the gulf near the town of Nuweiba (Klinger et al., 1999; Baer et al., 2008). Therefore, the co-seismic displacement field cannot be clearly isolated from secondary deformation processes after the earthquake. These challenges contribute to the uncertainties of estimated geodetic fault-slip models and probably in part explain the large differences between them (Supplement Tab. S2).

Seismic data analysis of the earthquake also faces challenges. At the time of the earthquake, the regional networks of seismic stations were sparse and seismic data were not easily shared between the four countries bordering the gulf (Saudi Arabia, Egypt, Israel, Jordan). Therefore, spatially uneven station geometry was used by the different agencies to locate the aftershock sequence of the earthquake (Hofstetter et al., 2003). Consequently, locations and faulting mechanisms of aftershocks are associated with large uncertainties (Abdel Fattah et al., 1997; Hofstetter et al., 2003).

With independent information on the location of the main fault rupture, identified and mapped based on data from a recent multibeam bathymetric survey (Ribot et al., 2021), with previously unused geodetic data, and applying multi-array teleseismic backprojection, we here derive a refined kinematic finite-fault rupture model for the Gulf of Aqaba earthquake using Bayesian inference combining geodetic and seismic data. This allows us to obtain a clearer picture of the rupture propagation during the earthquake.

## 2 Data and Methods

We use two main methods to study the rupture evolution of the 1995 Gulf of Aqaba earthquake: multi-array teleseismic backprojection (BP) and Bayesian kinematic earthquake source inference. We use the results obtained from the BP as a-priori information to parameterize the fault geometry and to constrain the parameter solution space for the source inference.

### 2.1 Multi-array backprojection

We applied multi-array teleseismic BP to image the spatio-temporal evolution of the rupture of the 1995 Aqaba earthquake. In traditional BP seismic recordings of a single array of seismic stations are windowed, aligned and stacked with respect to theoretical traveltimes calculated from a layered Earth structure model for a horizontal grid of potential source locations (Krüger and Ohrnberger, 2005; Ishii et al., 2005). This procedure involves no assumption on the fault geometry and allows space-time imaging of coherent seismic energy radiation (Kiser and Ishii, 2017) through so-called semblance maps. Note that semblance amplitudes have no direct physical relation to the amount of fault slip, but semblance maps indicate where radiated seismic energy of a certain slowness is coherently emitted. Coherent high-frequency seismic energy radiation is expected near the hypocenter in case of an energetic rupture onset and near asperities (patches of high slip), representing (abrupt) changes in earthquake rupture speed (Madariaga, 1977; Spudich and Frazer, 1984; Ide, 2002; Okuwaki and Yagi, 2018). Therefore, mapping the occurrence of high-frequency seismic radiation allows to highlight changes in the fault geometry and to assess the evolution and complexity of the earthquake rupture process independently from the source inversion. Instead of conducting a classical single large-array backprojection, we used multiple small-scale arrays for backprojection. Here, we outline the method only briefly, further details can be found in Steinberg et al. (2022).

We used a multi-array backprojection approach by clustering the available seismic stations using the k-means algorithm (Steinhaus, 1956) into many small virtual arrays (Rössler et al., 2010). We considered all globally available broad-band stations with waveform records between 23° and 93° distance from the earthquake epicenter, to have all near-field terms attenuated and to avoid triplications. Each virtual array has a unique set of stations and a minimum of 4 stations with a maximum array aperture of 3.5°. For the 1995 Gulf of Aqaba earthquake we ended up with 14 virtual arrays, with the smallest and largest arrays consisting of 4 and 26 stations, respectively (Fig. S1a). We only used the vertical component of velocity waveform records and backprojected with respect to the expected arrival times of the P-phase. Unfortunately, the sparse station configuration did not allow to also use the S-phase. We then calculated the semblance for each virtual array applying a phase-weighted stacking method (Schimmel and Paulssen, 1997). Semblance is a dimensionless mea-

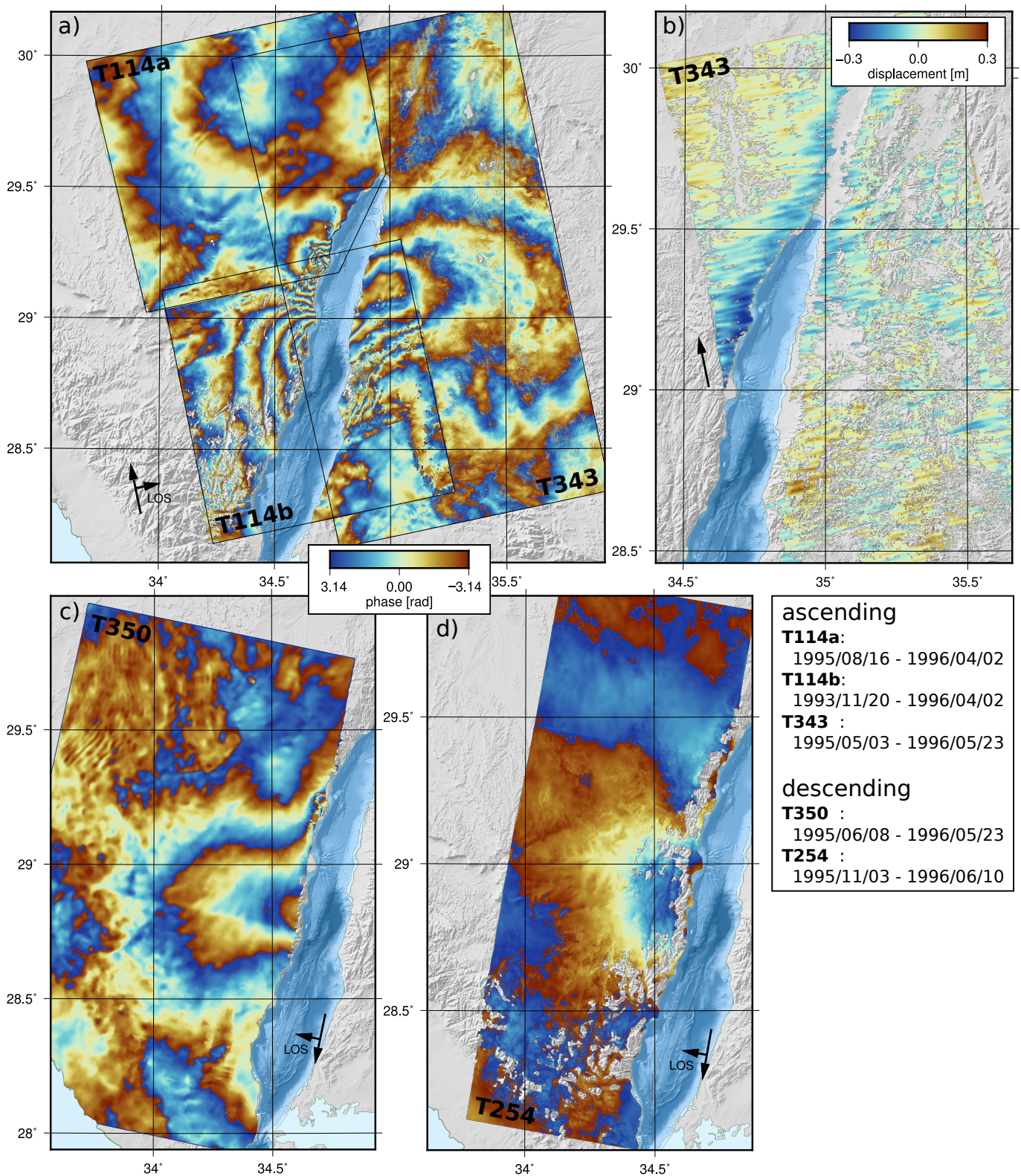


**Figure 2** a, c, d) Coseismic interferograms and b) azimuth pixel-offsets derived from SAR data (Supplement Tab. S1) and used for the fault geometry and finite-fault inference. Long and short arrows indicate the flight- and line-of-sight (LOS) directions of the satellite and the radar, respectively. Note that the data of track 254 are L-band data from the JERS-1, whereas the other are C-band data from the ERS-1/2 satellites. Bold black text labels indicate the satellite track numbers of the different datasets. The bottom right panel shows the primary and secondary SAR image acquisition dates for each track (format YYYY/MM/DD).

sure of coherence of waveforms at an array and can be multiplied, similar to a likelihood (Rössler et al., 2010). Therefore, we obtained the multi-array semblance by multiplication of all semblances (Steinberg et al., 2022).

Three-dimensional wave propagation effects that cannot be described by the assumed AK-135 1-D layered Earth structure model (Kennett and Engdahl, 1991) cause shifts in the wave arrival time and these in turn

bias the semblance map. To mitigate this effect and to reduce the absolute location error of the multi-array semblance map we estimate empirical travel time shifts and calibrate the waveform data before stacking at each station (Palo et al., 2014; Ishii et al., 2007; Meng et al., 2016; Fan and Shearer, 2017). We estimated these travel time shifts by maximizing the semblance for each virtual array based on a spatially close aftershock to the 1995 Gulf of Aqaba earthquake, the Mw 5.7 earthquake from 23.11.1995, 18:07:17 at  $29.333^{\circ}N, 34.749^{\circ}E$  (USGS location).

### 2.1.1 Configuration for the Gulf of Aqaba earthquake

For the Gulf of Aqaba earthquake we backprojected moving time windows of 6s length every 2s on point locations of a horizontal grid with a spacing of 0.05 degree ( $\sim 5$  km) at a depth of 18 km. We downsampled the seismic recordings to a common 10 Hz and we bandpass filtered the data, above the corner frequency of 0.15 Hz and up to 1.5 Hz. Following this process, we thus focus only on the high-frequency coherent emissions. The waveform records were then stacked for each time-step with respect to the calibrated theoretical arrival time for each considered grid point.

### 2.1.2 Backprojection uncertainty

To quantify the spatial and temporal accuracy of the multi-array BP results we follow a bootstrapping approach (Wang et al., 2016; Meng et al., 2012) on the semblance calculation at each timestep by perturbing seismic-wave travel times uniform randomly between  $\pm 2s$  for each virtual array and additionally between  $\pm 0.2s$  for each station. This process allows assessing the influence of wavepath effects on the multi-array semblance. We thus obtain an ensemble of bootstrapped multi-array semblance maps on which quantiles of semblance can be calculated. To document the uncertainties associated with the BP results we display multi-array semblance maps for each timestep, in which semblance maps show all possible coherent seismic-radiation locations for each timestep on the considered grid.

## 2.2 Bayesian kinematic finite fault inference

We use the Bayesian Earthquake Analysis Tool (BEAT, Vasyura-Bathke et al., 2019) and apply the step-wise inference strategy of Vasyura-Bathke et al. (2020) on surface-displacement maps derived from synthetic aperture radar (SAR) and on broadband teleseismic waveforms to infer distributions of earthquake source parameters that explain the observations within the range of associated uncertainty. First, based on geodetic and seismic data we estimate the geometry of the involved faults assuming rectangular planar fault-surfaces with uniform slip. Then, we use only the geodetic data to estimate spatially variable final (static) slip on the geometry of inferred faults. Finally, we use the thus obtained static slip distribution to inform the Bayesian inference for the kinematic rupture evolution

of the earthquake based on both the geodetic and seismic data, which we refer to as the finite-fault inference in the following.

Assuming a 1-D layered elastic half-space for the Earth structure (Khrepy et al., 2016), we calculate Green's functions (GFs) with 1 km spacing (Heimann et al., 2019) for the geodetic and the teleseismic data using the codes PSGRN/PSCMP (Wang et al., 2006) and QSSP (Wang et al., 2017), respectively. Sampling frequencies for the seismic GFs are 1 Hz and 4 Hz for the geometry and finite-fault inferences, respectively. To assess the fit of synthetic data  $\mathbf{d}_{syn}$  to the observed dataset  $\mathbf{d}_{obs}$  of waveforms and/or displacement maps we calculate the weighted variance-reduction (VR, Cohee and Beroza, 1994):

$$VR = \left( 1 - \frac{(\mathbf{d}_{obs} - \mathbf{d}_{syn})\mathbf{C}^{-1}(\mathbf{d}_{obs} - \mathbf{d}_{syn})}{\mathbf{d}_{obs}\mathbf{C}^{-1}\mathbf{d}_{obs}} \right) * 100 \quad (1)$$

where  $\mathbf{C}^{-1}$  is the inverse of the data covariance matrix. The closer the VR is to 100% the better the data are explained by the synthetics.

### 2.2.1 SAR data

We derived surface-displacement maps from five interferometric pairs of synthetic aperture radar (SAR) data and one SAR pixel offset map (Fig. 2) by using the GAMMA software (Wegmüller, 1998). Topographic phases have been evaluated and removed from the interferograms based on the SRTM digital elevation model (Farr et al., 2007). To increase the signal-to-noise ratio (SNR) the interferograms have been multilooked to  $\sim 90$  m x 90 m pixels and filtered with an adaptive phase filter (Goldstein and Werner, 1998). Finally, the filtered interferometric phases were unwrapped using a minimum cost flow algorithm (Chen and Zebker, 2001). To prepare the data for parameter inference, we reduced the number of pixels in the unwrapped interferograms by using the quadtree subsampling algorithm (Jónsson et al., 2002) and estimated the full data variance-covariance matrix following Sudhaus and Jónsson (2009) and Isken et al. (2017). The data from tracks 254 and 114 (Fig. 2) have not been used before in previous studies of this earthquake (Supplement Tab. S2). Note that due to irregular acquisition times (Supplement Tab. S1), the interferograms contain up to 24 and 21 months of pre- and post-seismic deformation, respectively. The influence of possible secondary sources of deformation on estimated parameters is discussed in sec. 4.3.

### 2.2.2 Teleseismic data

We used data from 27 broad-band seismic stations at teleseismic distances of  $26.5^{\circ} - 91.0^{\circ}$  and  $29.5^{\circ} - 87.0^{\circ}$  for the P and S wave data, respectively (Fig. S1,c & d). The data have been restituted to displacement and rotated to the radial, transverse and vertical (RTZ) source-receiver geometry. We applied band-pass filtering to contain waves with periods of 100s to 20s and 100s to 2s (i.e. band-pass filter between 0.01-0.05 Hz and 0.01-0.5 Hz) for the geometry and finite-fault inferences, respectively.

### 2.2.3 Inference of fault geometry

We estimated geometry and fault-slip kinematics of rectangular fault segments considering the following parameters for each fault segment: depth, length, width, slip, strike-, dip- and rake-angles. Assuming a half-cosinoidal source time function (STF, Lay et al., 2010) we also estimated nucleation-times and slip-duration of each fault segment. The top-center points of the fault segments have been fixed to be located on the mapped faults and surface ruptures of the earthquake (Ribot et al., 2021; Lefevre, 2018, i.e. faults annotated *AgF*, *AnF* and *mapped ruptures* in Fig. 1). In addition, we estimated hierarchical parameters for each interferogram, i.e. an offset and two ramp parameters (in the azimuth- and range directions) to mitigate effects of long wavelength atmospheric phase delays as well as inaccurate satellite orbit geometries. For the teleseismic data we estimated time shifts for each seismic station and waveform (P and S) to partially account for errors in the Green's Functions caused by lateral Earth-structure heterogeneities (Mustač et al., 2020; Vasyura-Bathke et al., 2021). We also estimated a noise-scaling parameter for each dataset residual to account for data and theory errors (Vasyura-Bathke et al., 2020, 2021). This setup yielded a total of 138 random variables, sampled from uniform distributions, to be constrained for the inference solution space which we explore using a sequential Monte-Carlo algorithm (Moral et al., 2006; Minson et al., 2013; Vasyura-Bathke et al., 2020).

### 2.2.4 Finite-fault inference

We employed the results from the geometry inference and fixed the fault segments geometry to the maximum a-posterior (MAP) solution. We then extended the fault segments in length and width in each direction, as fault dimensions are commonly underestimated applying the uniform-slip assumption, and discretized the fault segments with rectangular patches of 5.0 km. In total, we inferred >700 uniform distributed unknown parameters that comprise the slip in strike-parallel and down-dip directions, rupture duration, and rupture velocity on each patch. In addition, we estimated Laplacian smoothness regularization factors in conjunction with the location and time of separate rupture-nucleation points, i.e. one for each fault segment. We constrained the prior for the rupture-nucleation times for each fault segment based on a-priori information from the back-projection semblance maps. While we fixed the previously determined ramp parameters, we estimated noise-scaling factors for each dataset as well as the time shifts for each waveform applying sequential Monte Carlo sampling of the solution space.

## 3 Results

### 3.1 Backprojection source imaging

Our backprojection results (Fig. 3a) map several regions of coherent high-frequency seismic energy radiation moving from south to north along the Gulf of Aqaba.

The initial high-frequency energy was coherently radiated at -8 to -4 s with respect to gCMT time 04:15:26 near the southern end of the Aragonese fault (AgF), followed by an apparent gap of seismic radiation with a duration of around 6 s (Fig. 3). Subsequently, high-frequency energy was radiated on the adjacent northern continuation of the AgF at around 2-4 s and on the east coast of the Gulf at 4-6 s, nearby the observed surface fractures reported by Lefevre (2018). Finally, seismic radiation was again likely generated on the AgF migrating northward between 6-12 s. The high-frequency energy radiation at 10-12 s is possibly an artefact of the processing and discussed in detail in sec. 4.2.2.

### 3.2 Geometry of fault segments

We defined two fault-geometry setups, each with a different number of fault segments, to investigate the impact of additional source complexity for explaining the data. The first fault geometry comprises two fault segments: a single long off-shore segment on the AgF and a short on-shore segment located on the eastern gulf coast where surface ruptures have been mapped Lefevre (2018) and where we found coherent high-frequency energy radiation in the semblance maps (Fig. 3). The second fault-geometry setup comprises three fault segments, two shorter off-shore segments (on AgF and AnF) and the segment on the eastern shore (Fig. 3). We then estimate the fault geometric parameters, strike-angle, dip-angle, width and length, while other inferred parameters, such as slip, nucleation-time and slip-duration were included to not bias the estimation of the fault geometric parameters. Their inferred posterior probability densities (PPD) thus provide initial estimates only, as they were refined in the following finite-fault inference.

#### 3.2.1 Two fault segments

For the fault-model setup comprising two fault segments (Fig. 3a) the posterior ensembles show that the first segment (offshore, red) is well constrained. It dips  $\sim 70^\circ$ - $72^\circ$  towards west, and has length  $L$  of  $\sim 50$ - $53$  km and width  $W > 26$  km (Supplement Fig. S2). The second segment on the eastern shore of the Gulf (blue) is poorly constrained and dips  $\sim 80$  to  $90^\circ$  towards west. The PPD for fault length  $L$  (between 5 - 8km) is constrained by the prior information of the surface structures at the lower end of the distribution (Supplement Fig. S3). Whereas, the fault widths of above 9-10 km are more likely. The fault strike-angle was constrained to be between  $200$ - $210^\circ$  based on the a priori structural information, hence the PPD was truncated at  $200^\circ$ . While the offshore segment shows well constrained strike-slip motion (rake-angle of  $-7^\circ$  to  $-6^\circ$ ) the eastern segment shows mostly dip-slip (rake-angle of  $\leq -80^\circ$ ). The weighted variance reductions (VRs; Eq. 1) of the geodetic data are  $\sim 60\%$  for most of the interferometric pairs (Supplement Figs. S4, S5), but lower for the amplitude offsets that are overall noisy. Highest correlated residuals are located on the western shore of the Gulf. In general, the VRs for seismic data are high for P and S phases, i.e. between 75 - 95% (Supplement Figs. S6, S7). However, there are

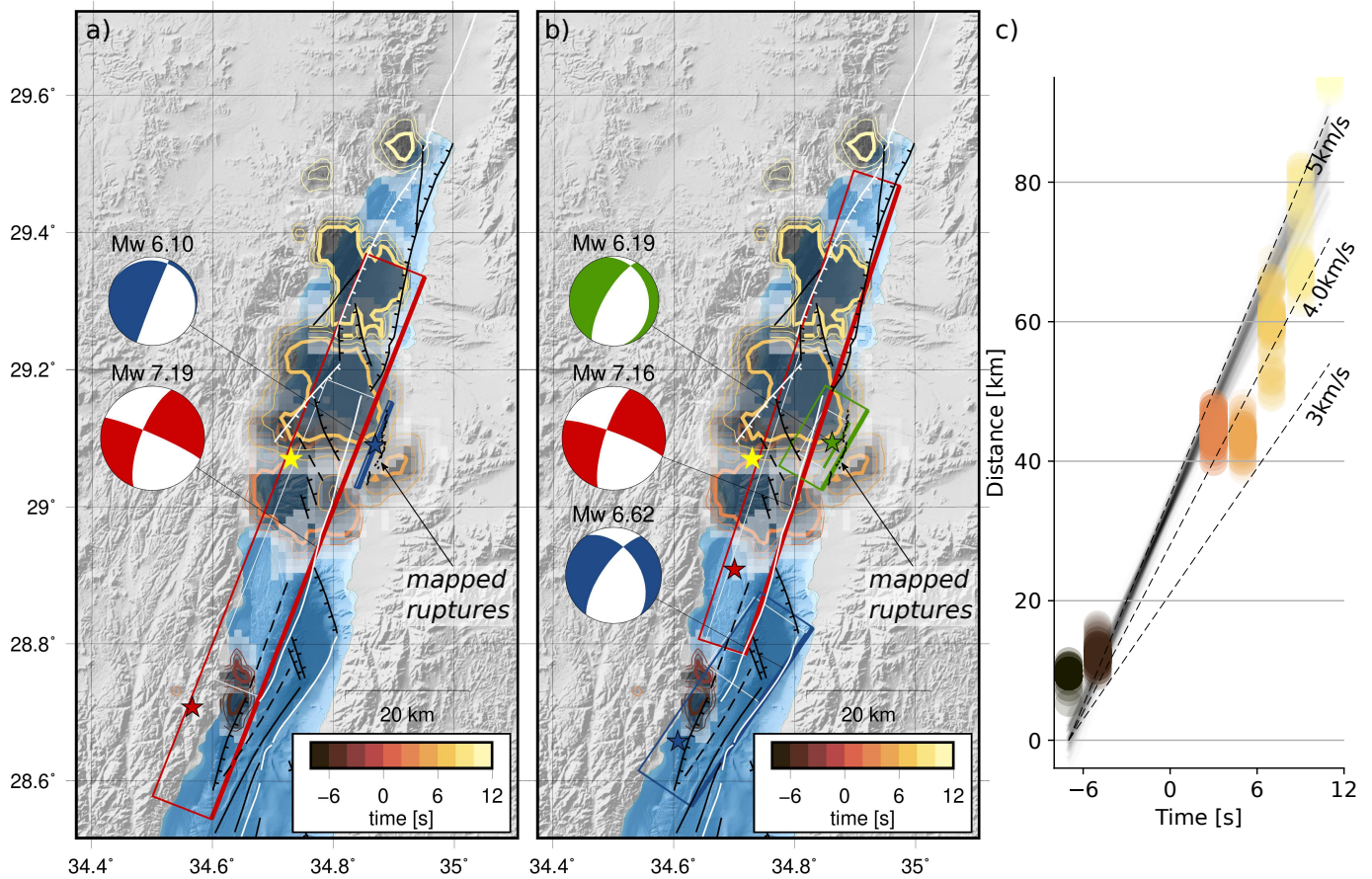


**Figure 3** Results of the backprojection analysis showing the temporal evolution of multi-array semblance with respect to the global centroid moment tensor time 04:15:26. Thick colored contour lines show the 90% quantile of the ensemble of multi-array semblances (white-to-gray areas), whereas thin contour lines indicate the subsequent 60% and 30% quantiles. Coloring and annotation of fault structures is identical to Fig.1, slightly modified after Lefevre (2018) and Ribot et al. (2021). The colored rectangles are the a) two and b) three fault segments used for the estimation of the rupture evolution, expanded in size from the estimated faulty geometry (thin gray rectangles), and the colored stars show the respective estimated rupture nucleation points on each segment. c) Ensemble of multi-array semblances projected along the axis of the gulf (strike of  $18^\circ$  East of North) referenced with respect to the earliest semblance between -8 and -6 s. Dashed black lines indicate steady rupture velocities of 3, 4 and 5  $km/s$  while shaded grey lines show averaged velocities for the whole ensemble of semblances.

a few stations that show remarkably low variance reductions, e.g. KMBO and BOSA (Fig. 4a).

### 3.2.2 Three fault segments

For the fault-geometry setup comprising three segments (Fig. 3b) the strike and dip angles of the northern segment (AgF) are well constrained at  $\sim 198^\circ$  and  $75 - 76^\circ$ , respectively. The strike- and dip-angles of the southern segment (AnF) hits the chosen upper bound of the prior distribution at  $215^\circ$  and  $70^\circ$  constrained by geologic information (Ribot et al., 2021, Figs. S8, S9). While the northern segment shows predominantly strike-slip motion, the southern segment (AnF) has a larger normal component of slip (rake-angle of  $\sim 50^\circ$  to  $-48^\circ$ ) compared to the northern segment (rake-angle of  $\sim 9^\circ$ ). The eastern on-shore segment (green) again shows predominantly normal slip (rake-angle of  $\sim 75^\circ$ ), Fig. S10). The variance-reduction (VR) values for three out of six geodetic datasets are higher by 5-12% (up to  $\sim 76\%$ ) compared to the two-segment geometry (Supplement Figs. S11 and S12). For the seismic data the variance reductions are in general only

slightly higher to those of the two-segment case. Stations KMBO.Z and BOSA.Z that showed low VRs for the two-segment setup have up to 70% higher variance reductions for the three-segment model. Moreover, other stations that show complexity in early P-phase arrivals (MSEY.Z, TATO.Z, HYB.Z) are explained significantly better in terms of amplitude and number of wave cycles, although in terms of VR these are only 5-7% higher (Fig. 4a). These improvements in VRs in comparison to the two-segments setup are significant and support the notion of geometrically complex faulting off-shore on the AnF and the AgF.

## 3.3 Finite-fault inference

### 3.3.1 Two fault segments

For the ensemble of two-segment finite-fault solutions, rupture initiates on the offshore segment at around -9.5 s to -8.2 s (wrt. gCMT time 04:15:26; Fig. 5a,b) between 25.5 km and 29.8 km depth, and then spreads unilaterally northeast across the segment. The onshore segment starts rupturing at  $\sim 8-8.9$  s, nucleating at shallow depth of around 1.0 km to 5.2 km and propagating

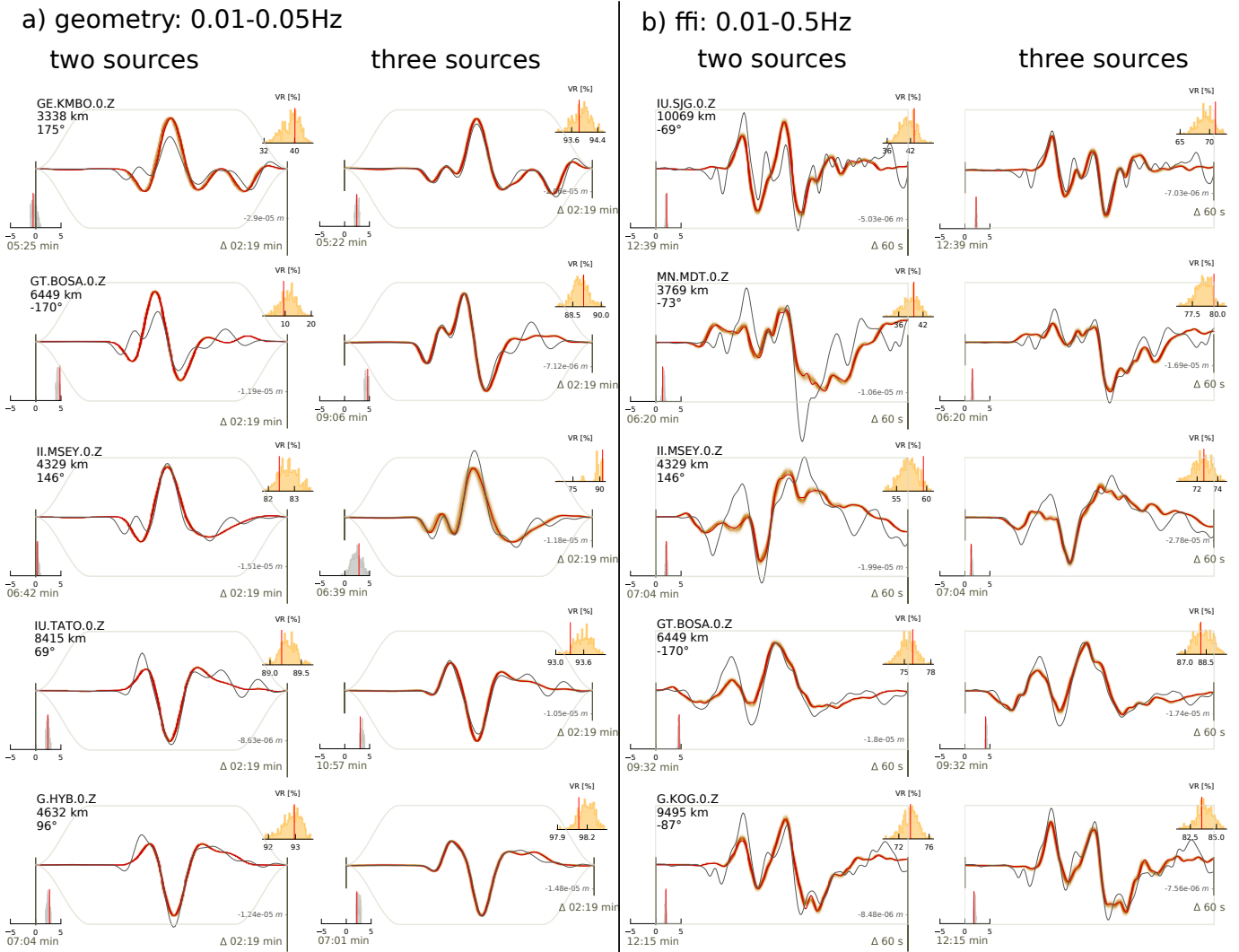


**Figure 4** Waveform fits of several selected stations for the a) geometry and b) finite-fault inversion inference of the 1995 Gulf of Aqaba earthquake. The solid gray lines show the filtered data of the vertical component tapered around the P-wave arrival. The red continuous lines show the synthetic waveforms derived from the MAP solution, whereas, brownish shaded colors indicate the synthetic waveforms derived from the full posterior ensemble of parameters.

unilaterally across the fault. The highest values of fault slip ( $> 1.8$  m) occur from the surface to a depth of  $\sim 9$  km on the central part of the offshore segment along a distance of  $\sim 25$  km. While fault motion is mostly strike-slip, some shallow slip with significant normal component is found. The timing and thus the velocity of the inferred rupture front towards north is consistent with the semblance maps from the BP, i.e. the rupture front reaches the region with high slip amplitude at  $\sim 4$  s. The moment-rate function reveals that seismic-moment release started gradually and linearly (Fig. 5a) and reached its maximum with several sharp peaks between  $\sim 6$ -8 s. This is followed by a fast decay of moment release until  $\sim 24$ -25 s. The geodetic data have an average VR of  $49.9 - 52.3\%$  (Supplement Figs. S15, S16), where the amplitude offsets with the highest noise show the lowest VR. Most noticeable residuals are again located on the western shore of the Gulf. Seismic data are well explained with an average VR of  $74.2 - 77.8\%$  (Supplement Figs. S17, S18). Here, both P and S phases are well modelled in general, but amplitudes of the main pulse and early P-phases are often biased resulting in

low VRs of  $36 - 60\%$ , e.g. SJG.Z, MDT.Z, MSEY.Z (Fig. 4b).

### 3.3.2 Three fault segments

In the ensemble of three-segment finite-fault solutions, rupture initiates on the southern segment at around  $-8.2$  s to  $-7.8$  s (wrt. gCMT time 04:15:26; Figs. 6a,b, 7) between 18.8 km and 22.5 km depth, and spreads unilaterally towards the Northeast across the segment. The second rupture then nucleates on the northern segment at  $\sim -1.5$  s to  $-1.1$  s between 19.3 km and 23.2 km depth and propagates in rather unilateral direction. Finally, the third, eastern segment starts rupturing between 3.7 s and 3.9 s at 4.7-9.4 km depth with unilateral rupture towards the down-dip direction (see also video in supplement). The slip is dominantly left-lateral on the southern and northern segments, but there is a notable normal component on all three segments (Fig. 6b). While the normal component is large at greater depths on the southern segment, it is high at shallow depths on the northern and eastern segments, respectively. The region with largest slip of  $> 1.8$  m, a length of  $\sim 25$  km

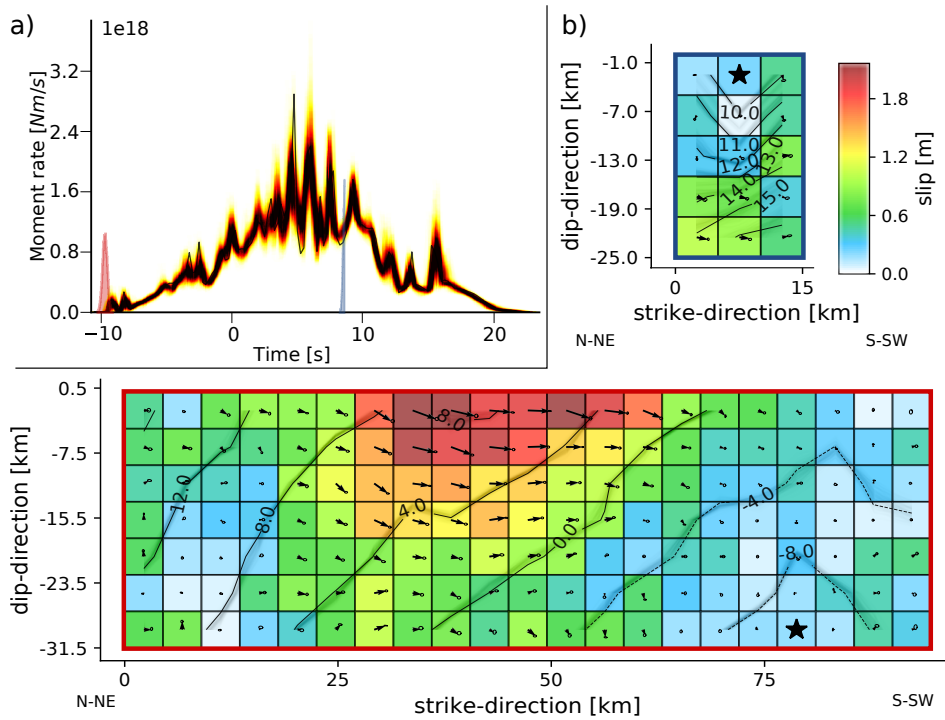


**Figure 5** Estimated spatiotemporal rupture evolution for the case with two fault segments. a) Ensemble of moment-rate functions with darker colors highlighting high-probability moment-rates. The maximum a-posterior moment rate is shown by the solid black line. Colored histograms (next to the moment-rate) show estimated rupture nucleation times of each fault-segment. b) Kinematic slip-distribution of the 1995 Gulf of Aqaba earthquake. Patch colors and arrows mark the MAP solution, whereas black ellipses mark the 95% standard deviation of slip. Black stars indicate the inferred rupture nucleation point on each fault segment and the black continuous lines show the MAP rupture front with the annotated timing. Uncertainty in rupture-front propagation is shown by fuzzy light-gray isolines indicating lower probability. All times are with respect to the global centroid moment tensor time 04:15:26.

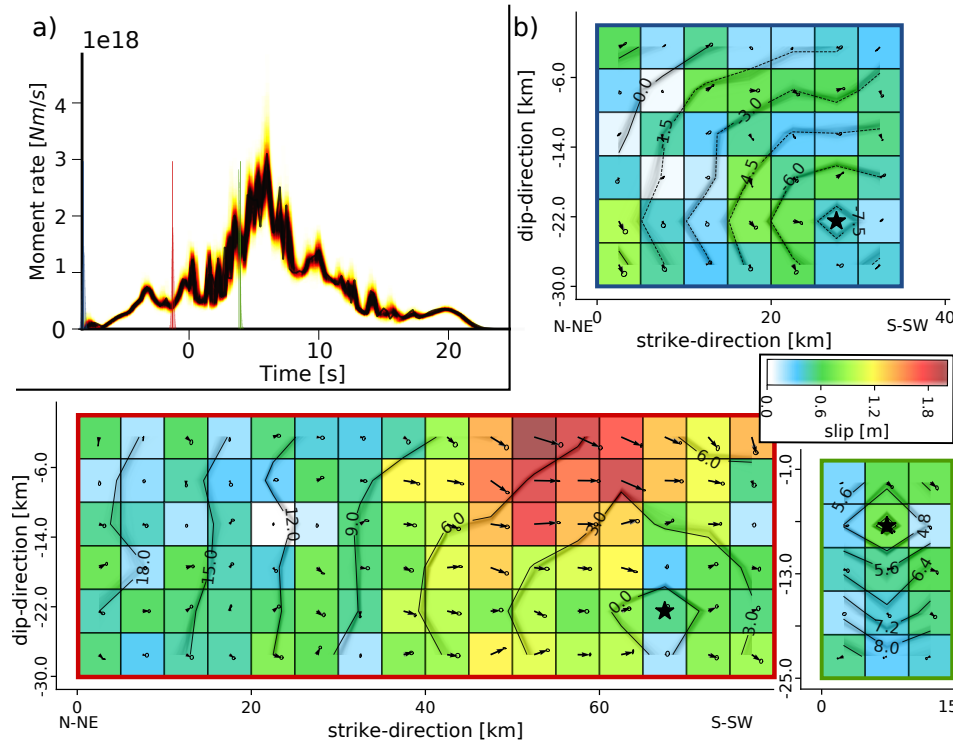


**Figure 6** Same as Fig. 5, except for the case of three fault segments.

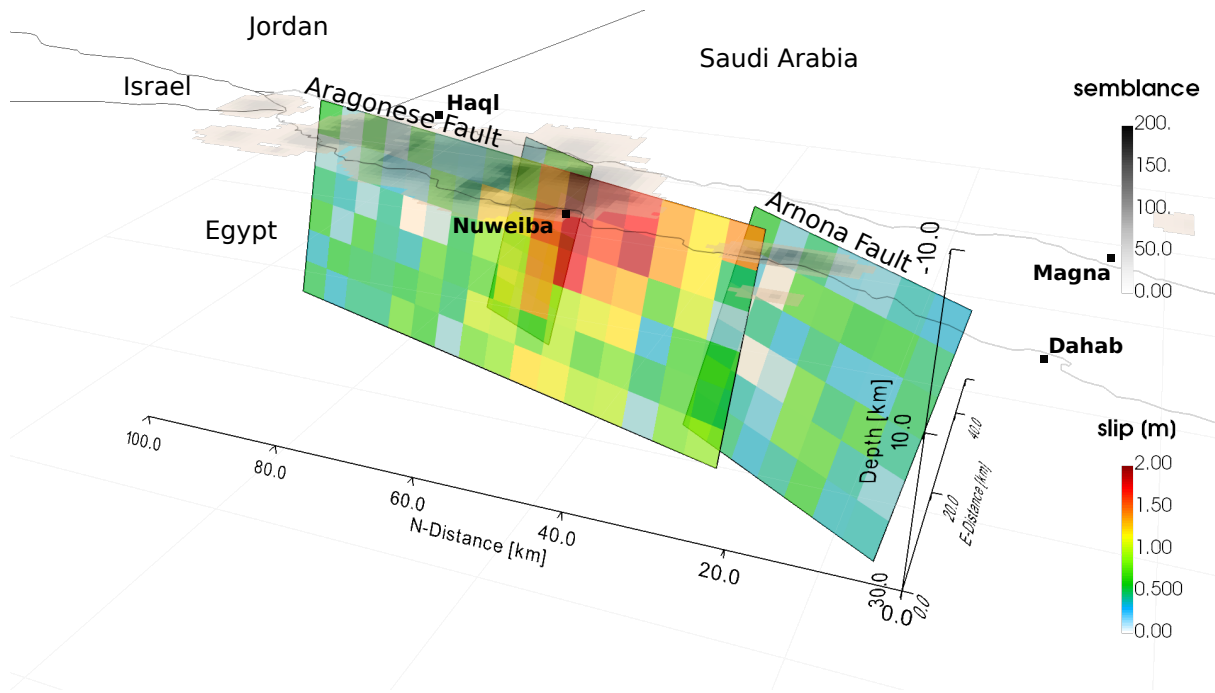


**Figure 7** Estimated slip-amplitude distribution for the three fault-segment case in 3D perspective view. Greyish colors show the back-projection semblance maps from Fig. 3. Thin black lines show coastlines and country borders. A video of the temporal rupture evolution can be found in the supplement.

and is located near the southern end of the northern segment, extending from the surface downwards to  $\sim 9$ – $15$  km depth. On the southern segment, maximum slip is  $\sim 1$  m close to the hypocentre at depths between 15 km and 22.5 km. The moment release started gradually and increased rapidly once the northern segment started rupturing (Fig. 6a). Most of the moment had been released at  $\sim 20$ s. The rupture velocity is noticeably faster on the southern segment  $\sim 3.2$ – $4.7$  km/s compared to that on the northern segment  $\sim 2.4$ – $3.5$  km/s. It is slowest on the eastern segment  $\sim 2.3$ – $3.7$  km/s (Figs. 6b, S19). In general, rupture velocity is better constrained close to the rupture nucleation points compared to further away.

Overall the geodetic data are slightly better explained by the three-segment model rather than by the two-segment setup with an average VR between 53.7–55.9%. The largest residuals are located on the western shore of the Gulf (Supplement Figs. S20, S21). Seismic data are similar or slightly better explained than for the two-segment model with an average VR between 77.7–80.1% (Supplement Figs. S22, S23). Most noticeable improvements (change in VRs between  $\sim 10$ – $40\%$ ) to the two-segment setup are for P-phases in the amplitudes of early arrivals e.g. SJG.Z, BOSA.Z, KOG.Z (Supplement Figs. S22) as well as for the main pulse, e.g. MDT.Z, MSEY.Z.

## 4 Discussion

We derived kinematic finite-fault rupture models for the 1995 Gulf of Aqaba earthquake that were estimated, to our knowledge, for the first time by the joint use of geodetic and seismic data through Bayesian inference. Taking into account only the ability of the presented

model(s) to explain the data in terms of variance reduction allows to reach a conclusive answer on the suitability of either the two or the three fault segment setups. While the three-segment setup only slightly better explains the geodetic data, it significantly better explains the seismic data. Calculating the Bayesian Information Criterion (BIC, Schwarz, 1978) for both models revealed that the three-segment configuration with 718 unknown parameters (153 patches) had a lower value than the two-segment configuration with 762 unknown parameters (162 patches). This result supports the use of the three fault segment configuration. Still, there are features in the two-segment geometry setup that are preferable to the other and vice versa. In the following section we discuss these features in detail.

### 4.1 Fault geometry

We find that geometric fault complexity approximated by the three-segment model is needed to explain especially early seismic phases. These indicate rupture on the northern end of the AnF, dipping westward towards the Aragonese Deep. For the gulf our inferred fault geometry shows a westward inclined segment along the entire fault length, although it was mapped in the south to be dipping eastward towards the Aragonese Deep and to be dipping westward towards the Elat Deep in the north (Ribot et al., 2021). Through forward modeling we tested the possibility for a vertical or eastward inclined southern end of the AgF segment (Fig. S24). It is highly unlikely that an eastward inclined fault has been activated during the earthquake as it would cause a clear data misfit on the eastern coast of the Gulf, assuming a fault segment dipping with  $80^\circ$  towards the East. Assuming a vertical fault segment does not cause as large a misfit to the geodetic data (Fig. S24a,b), but

the seismic data (Fig. S24c) is poorly explained on the Z-components. In conclusion, we propose that the Aragonese fault is curved in along-strike direction and that it is dipping westwards in the north and that it is subvertical close to the Aragonese Deep in the south. Depending on the amount of fault curvature on the inferred fault segments (which we assumed as planar in our models), the inferred distribution of slip may therefore be biased (Dutta et al., 2021).

## 4.2 Temporal rupture evolution

### 4.2.1 Artefacts in Finite Fault Inference

According to our source-inference results, several unilateral rupture fronts on the AnF and AgF, illustrated by the three-segment fault geometry, better explain the seismic data than a single unilateral rupture front involving only the AgF. However, there are second order features in the inferred kinematic finite fault setups that could rather be attributed to artifacts, potentially caused by theory error. Firstly, the deep rupture nucleation on the lower edges of the offshore faults in both fault-geometry models at depth  $> \sim 22\text{--}25$  km is rather unrealistic as the crustal thickness in the Gulf is reported to be  $\sim 20$  km. Secondly, the moment rate functions (Figs. 5a, 6a) show a long tail of moment release up to a total rupture duration of  $\sim 30$  s. This may be at least partially a result of the assumed sinusoidal functional form of the local source-time function on each fault patch (Meier et al., 2017). An alternative source-time function more consistent with earthquake rupture dynamics, e.g. the regularized Yoffee function (Tinti et al., 2005), may result in a shorter estimated total moment-rate function which would be more consistent with the apparent rupture duration of  $\sim 20$  s imaged by BP. Thirdly, the rupture velocity on the onshore segment for the two-segment setup is very slow  $\sim 2$  km/s and consequently, the rupture duration of that fault segment is long compared to its size (Kanamori and Brodsky, 2004). However, rupture-velocity and duration are source parameters which are potentially biased or influenced due to over-fitting to compensate some of the theory error. To improve this, the kinematic evolution of the rupture could be better resolved by utilising regional seismic data, which would likely reduce bias and artifacts in the estimated parameters.

### 4.2.2 Implications from back-projection

The employed BP method maps the coherent seismic radiation of P-wave energy related to changes in fault geometry and changes in rupture velocity, rather than the amount of fault-slip. Therefore, BP semblance is indicative of rupture nucleation, rupture arrest and kinks or bends in the fault geometry, however, the semblance values are not directly proportional to radiated seismic energy. The BP semblance map indicates a complex change of coherent energy radiation during the rupture process, and to first order resembles the inferred finite-fault models. Rupture velocities obtained from the BP results agree with those inferred in the finite-fault inversions: 3.3–3.7 km/s around the southern fault segment,

3.5–4.2 km/s around the northern fault segment and 2.8–3.3 km/s on the eastern fault segment.

One apparent discrepancy in the BP results compared to the inferred rupture models is the last mapped semblance at 18–20 s after rupture onset at the northern end of the AgF, onshore. These semblances may indicate that some fault segments in the north of the Gulf, such as the EF, slipped during the earthquake or that rupture was shallower or deeper than the depth of the grid used for the BP. No studies have reported a fault segment rupture this far north on the EF. Therefore, a mismatching of this semblance seems likely. Previous studies have shown that the choice of grid depth and the deviation of the source depth from the grid depth have a strong effect on the location of the mapped semblance (Steinberg et al., 2022; Daout et al., 2020), so this seems to be the likely cause. However, waveform coda and depth phases can also contaminate the BP results, especially in the later stages of the rupture process. In particular, depth phases may have relatively large amplitudes compared to direct phases, yet, for shallow earthquakes these phases arrive close in time in the seismic records. This results in unwanted side lobes either in parallel or at an acute angle to the fault depending on the station-array geometries. This effect can only be suppressed by using multi-phase semblance (Steinberg et al., 2022), which is hindered for the 1995 Gulf of Aqaba earthquake by limited data availability. Furthermore, the depth phase separation is challenging, particularly for strike-slip earthquakes that generate relatively large sP phases. Therefore, caution is necessary when interpreting the semblance maps of the later time steps in the BP.

To compare the two inferred kinematic finite-fault models to the BP results we carry out synthetic BPs on synthetic waveforms calculated by using the model parameters of the two- and three-segment finite-fault models (Fig. 8a, b). We used the same station setup and data processing as for the real data BP. Synthetic waveforms were calculated at a sample rate of 4 Hz using a Green's function store calculated with QSEIS and the AK-135 Earth structure model (Kennett and Engdahl, 1991). For both synthetic BPs we observe early bilateral rupture due to the abrupt stopping of the rupture at the model-fault edges. The observed semblance map of the real data BP at the northern end of the Gulf was not reproduced by the synthetic BP of either finite fault model.

The simple kinematic model used to calculate the synthetics produces sharper start and stop phases than actually observed (Steinberg et al., 2022), as the modelled fault ends abruptly, whereas in nature there would be tapering. Furthermore, the synthetic semblance maps produce much sharper semblance patches in comparison to the real data backprojection. The reason for this is due to the lack of data noise in the synthetic backprojection and, the fact that semblance is mapped onto a single fixed depth, which causes a blurred semblance in the real data backprojection.

In the synthetic BP of the two-segment finite-fault model the apparent rupture velocities are slow compared to the real data BP. The synthetic BP of the three-

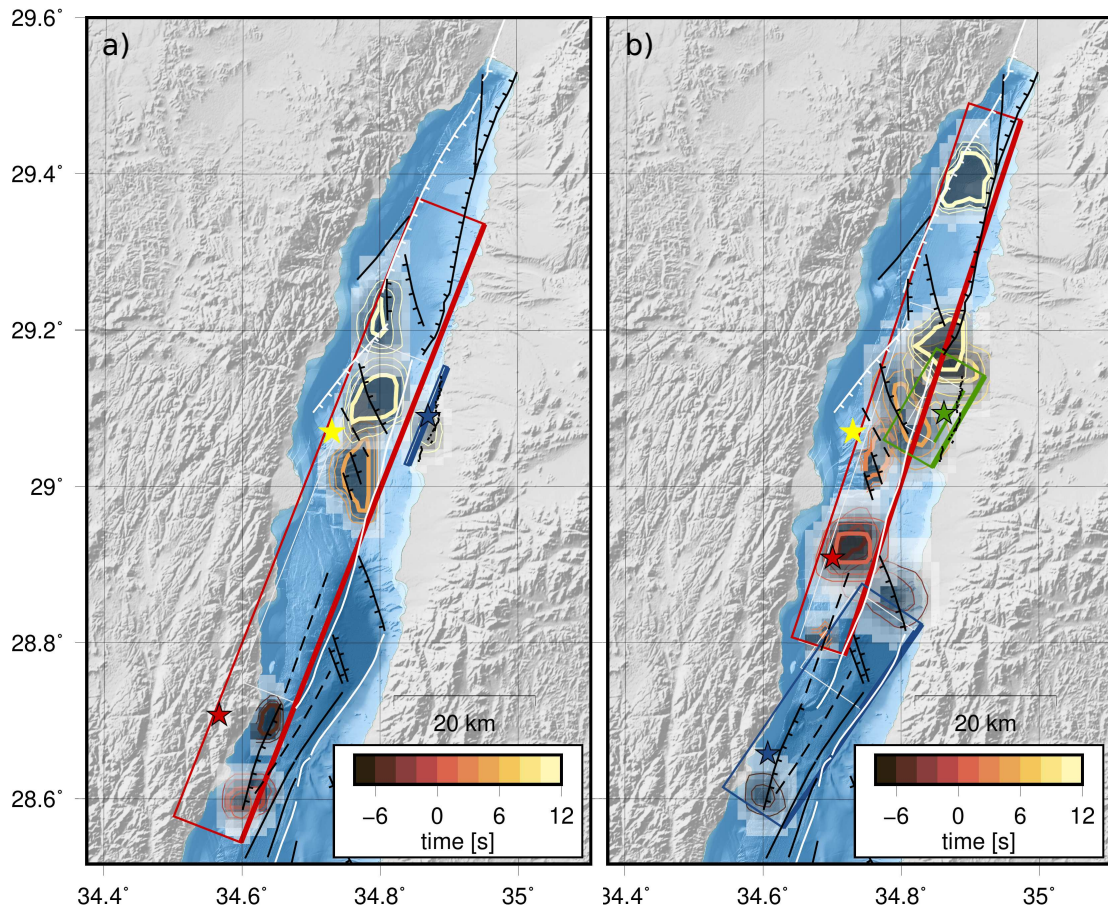


**Figure 8** Results of backprojection analysis of synthetic waveform data generated based on the MAP model of the a) two-segment and b) three-segment setups showing the temporal evolution of multi-array semblance with respect to the global centroid moment tensor time 04:15:26. Details are similar to Fig. 3

segment finite fault model (Fig. 8b) is in better agreement with the observed BP results (Fig. 3b), especially for the complicated semblance distribution in the center portion of the AgF. These probably indicate a change in rupture speed or fault geometry, e.g. in the form of a fault bend. The synthetic BP of the three fault segments also agrees well with observed complexity of semblance mapping in the area of the eastern fault segment.

#### 4.2.3 Rupture nucleation and fault segmentation

Our scenario with multiple rupture episodes, such as in the three-segment setup where rupture began on the AnF and subsequently propagated to the AgF, shows that rupture speed on the AnF is too slow for nucleation on the AgF to be triggered by unilateral rupture on the AnF or by the arrival of S-waves. The distance between the nucleation point on the AgF segment, which has a nucleation time of  $\sim 1.5$  s and the rupture front on the AnF segment at the same time, we estimate a rupture jumping distance between  $\sim 11$ -37 km. This is on the order of the 20 km jumping distance postulated for the 2016 Mw 7.8 Kaikoura earthquake (Cesca et al., 2017; Shi et al., 2017) and larger than previously proposed maximum jumping distances of 3-4 km (Wenousky, 2006). However, the rupture nucleation on the AgF could have been caused by dynamic triggering of P-waves emitted during the early stages of the AnF seg-

ment rupture. The P-wave velocity is between  $\sim 6.5$  and  $6.9$  km/s (Khrepy et al., 2016), such that a theoretical travel-time of  $\sim 3.5$ -5.5 s would be required between nucleation points (Fig. 9; distance of 27-32 km). The difference between inferred nucleation times in our three-segment setup as well as the temporal difference between the BP semblance maps are  $\sim 6$ -7 s (Figs. 3-5), and thus they are within a plausible range for this required travel time. Using QSEIS we simulated the seismic wavefield generated by slip on all patches of the first fault-segment and then received at the second nucleation point. This allows for estimating the dynamic Coulomb stress imposed at the nucleation point on the second fault segment (Fig. 9). The second rupture on the northern segment initiated at a Coulomb stress change of  $\sim 0.3$  MPa which is consistent with previously reported dynamic Coulomb stress changes needed to trigger earthquake rupture (e.g. Antonioli et al., 2006). Thus, it seems plausible that rupture on the AgF segment was triggered by the early pulses of deformation associated with the seismic phases that have been emitted from the AnF segment. Another possibility is that a small, unresolved normal-fault segment acted as an intermediary and facilitated an apparent jump of the rupture. However, this would require that the rupture process on this small normal-fault segment was very smooth and did not emit any start or stop phases that could be resolved through backprojection using the available data.

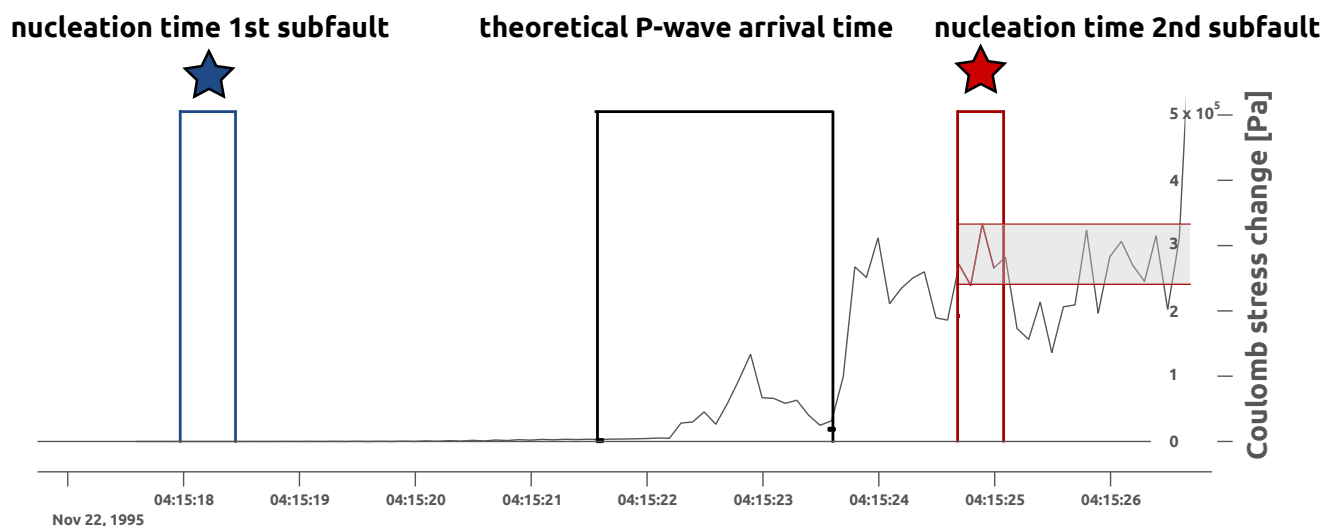


**Figure 9** Time-dependent Coulomb stress changes at the second nucleation point of the three-segment fault geometry imposed by all source patches from the southern fault segment. The blue and red boxes mark the uncertainty of the inferred nucleation time of the southern and northern fault segments, respectively. The area indicated by the black box marks the window of theoretical P-wave arrival times (for the posterior ensemble of models) for a P-wave traveling from the hypocenter to the second nucleation point on the northern fault-segment. The shaded grey box marks the interval of inferred Coulomb stress-change during the initiation time of the northern fault segment.

### 4.3 Secondary sources of deformation

Residual displacements of pixel offsets and interferograms are in general relatively high (Supplement Figs. S11, S12), especially on the western coast of the Gulf. On the other hand, residuals of seismic waveforms are low (Figs. S17, S18, S22, S23). Interferometric pairs cover significant time-spans where the secondary acquisitions have been acquired 5-6 months after the mainshock (Supplement Tab. S1). During this time, post-seismic deformation processes have occurred that are not included in the presented co-seismic kinematic finite-fault models. Especially, four shallow normal faulting aftershocks with magnitudes  $M_w \geq 3.9$  (Baer et al., 2008, Supplement Tab. S2) have been reported (Hofstetter et al., 2003) on the western coast of the Gulf where the large residual deformation is present in the SAR data (Figs. 1, S20, S21). In conjunction with post-seismic deformation such as afterslip (Baer et al., 2008) these can account for  $\sim 5$ -7 cm of displacement, which is the bulk part of residual displacements in the interferograms. Thus, the joint inference of seismic and geodetic data played an important role for disseminating the contribution of these signals.

### 4.4 Ground-motion map from finite fault inference

The surface effects of an earthquake on infrastructure and population are typically evaluated using ground motion maps. The inferences from our finite fault modelling of the 1995 Aqaba earthquake can be used to produce an informed estimate of realistic peak-ground velocity (PGV) predictions for this particular earthquake. These may then serve as a basis for scenario calculations for seismic hazard assessment in the region.

We calculated a deterministic physics-based ground-

motion map by simulating the seismic wavefield based on the spatiotemporal rupture evolution of the three-segment fault model (Fig. 6, Dahm et al., 2018). For the wavefield simulation we calculate Green's functions with QSEIS (Wang, 1999) with a sample rate of 20 Hz at a dense set of virtual receivers (1 km spacing) assuming the 1D-layered elastic Earth structure model used also in our FFI (Khrepy et al., 2016). We considered site effects through the shear-wave velocity in the thirty meters below Earth surface,  $V_{s30}$ , derived from the topographic slope as a proxy (Wald and Allen, 2007). We calculate the amplification ratio  $A_{30}$  between the predicted  $V_{s30}$  and the shear-wave velocity of the uppermost layer resulting from our Green's functions. After bandpass filtering the simulated waveforms between 1-8 Hz and subsequent rotation to the RTZ coordinate system the expected PGV at each grid point is calculated from the maximum of the geometric mean of the absolute horizontal components R and T (Wald and Allen, 2007). The predicted PGV's (Fig. 10) close to the source region reach 2 m/s. Adjacent areas at intermediate distances of  $\sim 20$  km perpendicular to the source region of the main active fault (red), which has the highest inferred amount of slip, still have predicted PGV values of up to 0.5 m/s. The rupture directivity of the Gulf of Aqaba earthquake was toward north, and hence the shaking in the northern gulf is stronger than in the southern gulf and adjacent coastal regions.

### 4.5 Comparison to published models

Earlier studies (Pinar and Türkelli, 1997; Klinger et al., 1999; Hofstetter et al., 2003; Shamir et al., 2003; Baer et al., 2008) modelled the Aragonese fault as a single planar fault, similar to the offshore segment of our two-segment fault geometry setup. In published finite-fault

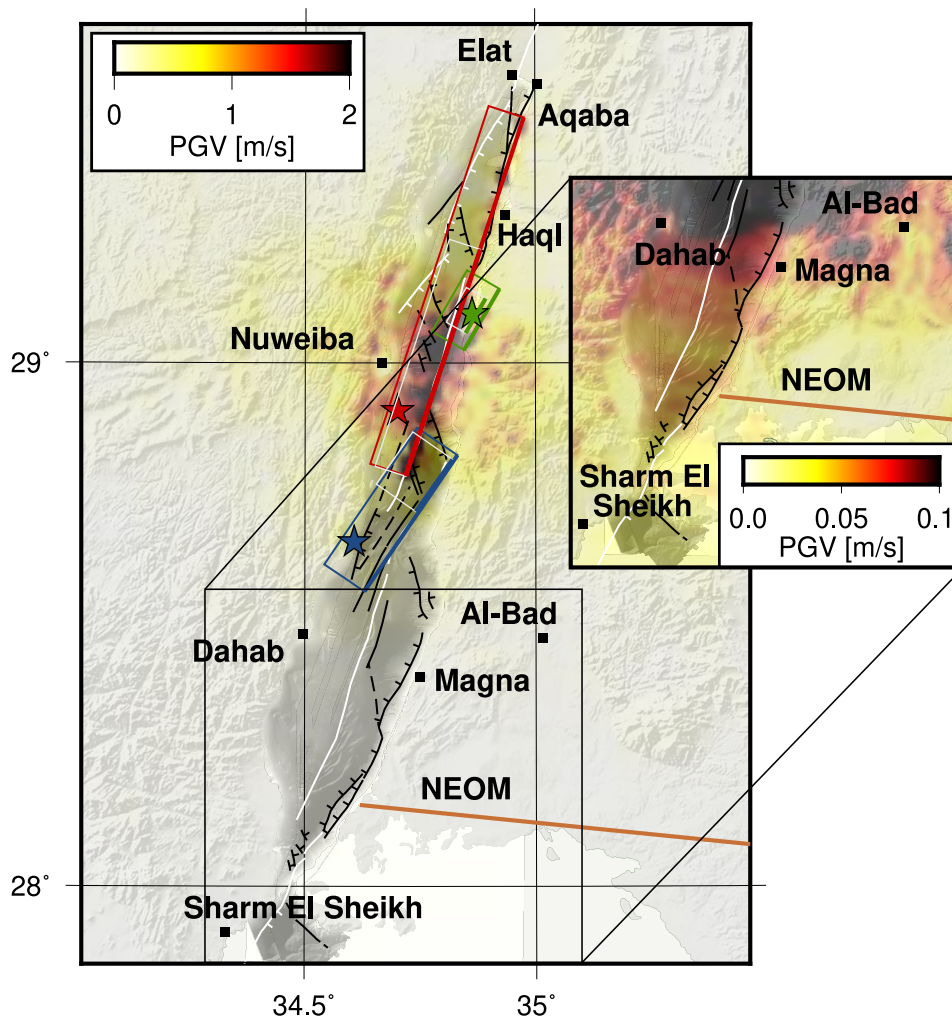


**Figure 10** Map of estimated peak ground velocity (PGV) from seismic wavefield simulation (frequency range 1-8 Hz) for our three-segment rupture model of the 1995 Gulf of Aqaba earthquake. The colored rectangles mark the three fault segments. The black rectangle shows the zoom-in around the area of the urban project NEOM; note the different scale of colormap in the zoom-in. "The Line" (brown) is a  $\sim 170$  km long city under construction. Coloring and annotation of fault structures is identical to Fig.1.

slip models the large-slip area is located at depth between 5 and 15 km and peak slip-amplitudes are larger by  $\sim 1$  m (Hofstetter et al., 2003; Baer et al., 2008) compared to our result (Fig. 5b, 6b). In contrast to published models our slip models show a notable component of normal slip at shallow depths to  $\sim 8$  km depth. While our findings are in line with most of the previous studies that the earthquake consisted of several sub-events (Fig. 1, Supplement Tab. S2), they differ in the locations of the sub-events (Pinar and Türkelli, 1997; Klinger et al., 1999). While our three-segment model supports the proposed hypothesis that rupture initiated on the AnF in the south and then jumped to the AgF it does not support continued jumping to the EF in the north. Our results support that the deformation on the western coast of the Gulf was largely due to post-seismic deformation and aftershocks (Baer et al., 2008) rather than co-seismic mainshock slip. This post-seismic activity was predominantly characterised by vertical surface displacements, i.e. subsidence 20 km north of Nuweiba (Fig. S25). Furthermore, we propose that a fault segment on the eastern shore of the Gulf was active during the mainshock. Although, the inference of tele-

seismic and geodetic data do not allow to constrain this segment well, the BP results and the mapped structures (Fig. 1) indicate active faulting there. All these findings, i.e. shallow normal slip, normal faulting sub-event on the eastern shore and post-seismic normal faulting on the western shore are indicative of active tectonic extension during and after the Gulf of Aqaba earthquake.

While the inferred moment-rate function of our two-segment setup is similar to the one obtained by Hofstetter et al. (2003), i.e. roughly triangular symmetric with a rupture duration of  $\sim 25$  s; the inferred moment-rate function for our three-segment setup is more similar to that of Pinar and Türkelli (1997). The total estimated moment magnitudes of our two and three-segment models are 7.24 and 7.27, respectively, which is slightly greater than previous estimates of 7.04-7.21 (Tab. S1).

## 5 Conclusions

We imaged the rupture of the 1995 Gulf of Aqaba earthquake using teleseismic multi-array backprojection. Mapped fault structures were used as prior infor-

mation to constrain the location of activated faults in the gulf. We also estimated the kinematic finite-fault rupture evolution of the Aqaba 1995 earthquake using geodetic and teleseismic data jointly within a Bayesian inference process. We find that most of the rupture has occurred on the offshore west-dipping Aragonese fault which is curved in the along-strike direction. However, rupture initiated on the west-dipping Arnona fault south of the Aragonese fault. The temporal rupture evolution is complex and the inversion results support unilateral rupture originating close to the northern end of the Arnona fault and jumping over to the Aragonese fault that then again ruptured unilaterally towards the north. The backprojection results support this case. The earlier rupture in the south could have dynamically triggered the rupture on the Aragonese fault. In contrast to earlier studies we argue that a small on-shore fault segment on the eastern coast of the gulf was seismically active during the event. While the event was predominantly strike-slip our models show that a significant portion of normal slip must have occurred along the Arnona and Aragonese faults. In conjunction with the sub-event on the eastern shore and post-seismic normal faulting on the western shore, our results suggest active tectonic extension of the gulf. Overall, this study presents new earthquake rupture models that describe the temporal rupture evolution of the 1995 Gulf of Aqaba earthquake. Especially, the postulated dynamic triggering between the fault segments should be taken into account for hazard models in the area, as this shows that seismic moment can be released faster over a shorter amount of time than during a purely unilateral rupture. Given large infrastructure projects such as NEOM that are actively being developed in vicinity of the Gulf of Aqaba with its geometrically complicated active fault system, the modelling of earthquakes in the region is important for updated and informed hazard assessment and for establishing scenarios of potential future earthquakes.

## 6 Acknowledgements

The authors thank František Gallovič, an anonymous reviewer and the editors for their comments which helped to improve the quality of the manuscript. HVB thanks Nicolas Castro-Perdomo for providing shapefiles of structures around the Dead Sea fault. This research was supported by King Abdullah University of Science and Technology (KAUST), under award numbers BAS/1/1353-01-01, BAS/1/1339-01-01, and OSR-CRG2020-4335. H.V-B was partially supported by Geo.X, the Research Network for Geosciences in Berlin and Potsdam under the project number SO\_087\_GeoX. A.S. was partially supported by the German Research Foundation DFG through an Emmy-Noether Young-Researcher-Grant (Number 276464525, "Bridging Geodesy and Seismology for improved and automated estimation of faulting events").

## Data and code availability

The facilities of IRIS Data Services, and specifically the IRIS Data Management Center, were used for access to waveforms, related metadata, and/or derived products used in this study under <https://ds.iris.edu>. IRIS Data Services are funded through the Seismological Facilities for the Advancement of Geoscience (SAGE) Award of the National Science Foundation under Cooperative Support Agreement EAR-1851048. The post-processed InSAR data are available for download at <https://zenodo.org/records/10462416> (Vasyura-Bathke et al., 2024). Bayesian inferences and multi-array teleseismic backprojection were performed using the Bayesian Earthquake Analysis Tool (BEAT; <https://github.com/hvasbath/beat>, Vasyura-Bathke et al., 2019, 2020) and Palantiri (<https://github.com/braunfuss/Palantiri>) (Steinberg, 2021; Steinberg et al., 2022), respectively. This work employed the open source libraries: *Numpy* (Harris et al., 2020), *Scipy* (Virtanen et al., 2020), *pyrocko* ([www.pyrocko.org](http://www.pyrocko.org)) (Heimann et al., 2017). Plots have been produced by using *Matplotlib* (Hunter, 2007) and the Generic Mapping Tools (GMT) (Wessel et al., 2013).

## References

- Abdel Fattah, A. K., Hussein, H. M., Ibrahim, E. M., and Abu El Atta, A. S. Fault plane solutions of the 1993 and 1995 Gulf of Aqaba earthquakes and their tectonic implications, 1997. doi: 10.4401/ag-3831.
- Antonoli, A., Belardinelli, M. E., Bizzarri, A., and Vogfjord, K. S. Evidence of instantaneous dynamic triggering during the seismic sequence of year 2000 in south Iceland. *J. Geophys. Res. Solid Earth*, 111(3):1–14, 2006. doi: 10.1029/2005JB003935.
- ArRajehi, A., McClusky, S., Reilinger, R., Daoud, M., Alchalbi, A., Ergintav, S., Gomez, F., Sholan, J., Bou-Rabee, F., Ogubazghi, G., Haileab, B., Fisseha, S., Asfaw, L., Mahmoud, S., Rayan, A., Bendik, R., and Kogan, L. Geodetic constraints on present-day motion of the Arabian Plate: Implications for Red Sea and Gulf of Aden rifting. *Tectonics*, 29:TC3011, 2010. doi: 10.1029/2009TC002482.
- Baer, G., Shamir, G., Sandwell, D., and Bock, Y. Crustal deformation during 6 years spanning the  $M_w = 7.2$  1995 Nuweiba earthquake, analyzed by Interferometric Synthetic Aperture Radar. *Israel Journal of Earth Sciences*, 50(1):9–22, 2001. doi: 10.1560/12MA-85HY-WHXL-0GKA.
- Baer, G., Funning, G. J., Shamir, G., and Wright, T. J. The 1995 November 22,  $M_w 7.2$  Gulf of Elat earthquake cycle revisited. *Geophys. J. Int.*, 175(3):1040–1054, dec 2008. doi: 10.1111/j.1365-246X.2008.03901.x.
- Ben-Avraham, Z. Structural framework of the Gulf of Elat (Aqaba), Northern Red Sea. *J. Geophys. Res.*, 90:703–726, 1985. doi: 10.1029/JB090iB01p00703.
- Castro-Perdomo, N., Viltres, R., Masson, F., Klinger, Y., Liu, S., Dhahry, M., Ulrich, P., Bernard, J.-D., Matrau, R., Allothman, A., Zahran, H., Reilinger, R., Mai, P. M., and Jónsson, S. Interseismic deformation in the Gulf of Aqaba from GPS measurements. *Geophys. J. Int.*, 228:477–492, 2022. doi: 10.1093/gji/ggab353.
- Cesca, S., Zhang, Y., Mouslopoulou, V., Wang, R., Saul, J., Savage, M., Heimann, S., Kufner, S. K., Oncken, O., and Dahm, T. Complex rupture process of the  $M_w 7.8$ , 2016, Kaikoura earthquake, New Zealand, and its aftershock sequence. *Earth Planet. Sci. Lett.*, 478:110–120, 2017. doi: 10.1016/j.epsl.2017.08.024.

- Chen, C. W. and Zebker, H. A. Two-dimensional phase unwrapping with use of statistical models for cost functions in nonlinear optimization. *J. Opt. Soc. Am. A*, 18:338–351, 2001. doi: 10.1364/JOSAA.18.000338.
- Cohee, B. P. and Beroza, G. C. Slip distribution of the 1992 Landers earthquake and its implications for earthquake source mechanics. *Bulletin of the Seismological Society of America*, 84(3): 692–712, 06 1994. doi: 10.1785/BSSA0840030692.
- Dahm, T., Heimann, S., Funke, S., Wendt, S., Rappsilber, I., Bindi, D., Plenefisch, T., and Cotton, F. Seismicity in the block mountains between Halle and Leipzig, Central Germany: centroid moment tensors, ground motion simulation, and felt intensities of two M3 earthquakes in 2015 and 2017. *J. Seismol.*, 22(4): 985–1003, 2018. doi: 10.1007/s10950-018-9746-9.
- Daout, S., Steinberg, A., Isken, M. P., Heimann, S., and Sudhaus, H. Illuminating the Spatio-Temporal Evolution of the 2008–2009 Qaidam Earthquake Sequence with the Joint Use of Insar Time Series and Teleseismic Data. *Remote Sensing*, 12(17):2850, 2020. doi: 10.3390/rs12172850.
- Dutta, R., Jónsson, S., and Vasyura-Bathke, H. Simultaneous Bayesian Estimation of Non-Planar Fault Geometry and Spatially-Variably Slip. *J. Geophys. Res. Solid Earth*, 126(7):1–28, 2021. doi: 10.1029/2020JB020441.
- Fan, W. and Shearer, P. M. Investigation of backprojection uncertainties with M6 earthquakes. *J. Geophys. Res. Solid Earth*, 122(10):7966–7986, 2017. doi: 10.1002/2017JB014495.
- Farr, T. G., Rosen, P. A., Caro, E., Crippen, R., Duren, R., Hensley, S., Kobrick, M., Paller, M., Rodriguez, E., Roth, L., Seal, D., Shaffer, S., Shimada, J., Umland, J., Werner, M., Oskin, M., Burbank, D., and Alsdorf, D. The shuttle radar topography mission. *Rev. Geophys.*, 45(2005):1–33, 2007. doi: 10.1029/2005RG000183.
- Goldstein, R. M. and Werner, C. L. Radar interferogram filtering for geophysical applications. *Geophys. Res. Lett.*, 25(21): 4035–4038, nov 1998. doi: 10.1029/1998GL900033.
- Harris, C. R., Millman, K. J., van der Walt, S. J., Gommers, R., Virtanen, P., Cournapeau, D., Wieser, E., Taylor, J., Berg, S., Smith, N. J., Kern, R., Picus, M., Hoyer, S., van Kerkwijk, M. H., Brett, M., Haldane, A., del Río, J. F., Wiebe, M., Peterson, P., Gérard-Marchant, P., Sheppard, K., Reddy, T., Weckesser, W., Abbasi, H., Gohlke, C., and Oliphant, T. E. Array programming with NumPy. *Nature*, 585(7825):357–362, sep 2020. doi: 10.1038/s41586-020-2649-2.
- Heimann, S., Kriegerowski, M., Isken, M., Cesca, S., Daout, S., Grigoli, F., Juretzek, C., Megies, T., Nooshiri, N., Steinberg, A., Sudhaus, H., Vasyura-Bathke, H., Willey, T., and Dahm, T. Pyrocko - An open-source seismology toolbox and library. *GFZ Data Services*, v. 0.3, 2017. doi: http://doi.org/10.5880/GFZ.2.1.2017.001.
- Heimann, S., Vasyura-Bathke, H., Sudhaus, H., Isken, M. P., Kriegerowski, M., Steinberg, A., and Dahm, T. A Python framework for efficient use of pre-computed Green's functions in seismological and other physical forward and inverse source problems. *Solid Earth*, 10(6):1921–1935, 2019. doi: 10.5194/se-10-1921-2019.
- Hofstetter, A., Thio, H. K., and Shamir, G. Source mechanism of the 22 / 11 / 1995 Gulf of Aqaba earthquake and its aftershock sequence. *J. Seismolog.*, 7:99–114, 2003. doi: 10.1023/A:1021206930730.
- Hunter, J. D. Matplotlib : A 2D graphics environment. *Comput. Sci. Eng.*, 9(3):90–95, 2007. doi: 10.1109/MCSE.2007.55.
- Ide, S. Estimation of radiated energy of finite-source earthquake models. *Bull. Seismol. Soc. Am.*, 92(8):2994–3005, 2002. doi: 10.1785/0120020028.
- Ishii, M., Shearer, P. M., Houston, H., and Vidale, J. E. Extent, duration and speed of the 2004 Sumatra-Andaman earthquake imaged by the Hi-Net array. *Nature*, 435(7044):933–936, 2005. doi: 10.1038/nature03675.
- Ishii, M., Shearer, P. M., Houston, H., and Vidale, J. E. Teleseismic P wave imaging of the 26 December 2004 Sumatra-Andaman and 28 March 2005 Sumatra earthquake ruptures using the Hi-net array. *J. Geophys. Res. Solid Earth*, 112(B11), 2007. doi: 10.1029/2006JB004700.
- Isken, M., Sudhaus, H., Heimann, S., Steinberg, A., Daout, S., and Vasyura-Bathke, H. Kite - Software for Rapid Earthquake Source Optimisation from InSAR Surface Displacement. *GFZ Data Services*, v 0.1, 2017. doi: http://doi.org/10.5880/GFZ.2.1.2017.002.
- Jónsson, S., Zebker, H., Segall, P., and Amelung, F. Fault slip distribution of the 1999 Mw 7.1 Hector Mine, California, earthquake, estimated from satellite radar and GPS measurements. *Bull. Seismol. Soc. Am.*, 92(4):1377–1389, 2002. doi: 10.1785/0120000922.
- Kanamori, H. and Brodsky, E. E. The physics of earthquakes. *Rep. Prog. Phys.*, 67(8):1429–1496, 2004. doi: 10.1088/0034-4885/67/8/R03.
- Kennett, B. and Engdahl, E. Traveltimes for global earthquake location and phase identification. *Geophys. J. Int.*, 105(2): 429–465, 1991. doi: 10.1111/j.1365-246X.1991.tb06724.x.
- Khrepy, S. E., Koulakov, I., Al-Arifi, N., and Petrunin, A. G. Seismic structure beneath the Gulf of Aqaba and adjacent areas based on the tomographic inversion of regional earthquake data. *Solid Earth*, 7(3):965–978, 2016. doi: 10.5194/se-7-965-2016.
- Kiser, E. and Ishii, M. Back-Projection Imaging of Earthquakes. *Annu. Rev. Earth Planet. Sci.*, 45:271–299, 2017. doi: 10.1146/annurev-earth-063016-015801.
- Klinger, Y., Rivera, L., Haessler, H., and Maurin, J.-c. Active Faulting in the Gulf of Aqaba : New Knowledge from the Mw 7.3 Earthquake of 22 November 1995. *Bull. Seismol. Soc. Am.*, 89(August): 1025–1036, 1999. doi: 10.1785/BSSA0890041025.
- Klinger, Y., Michel, R., and Avouac, J.-P. Co-seismic deformation during the Mw 7.3 Aqaba earthquake ( 1995 ) from ERS-SAR interferometry. *Geophys. Res. Lett.*, 27(22):3651–3654, 2000. doi: 10.1029/1999GL008463.
- Krüger, F. and Ohrnberger, M. Tracking the rupture of the Mw = 9.3 Sumatra earthquake over 1,150 km at teleseismic distance. *Nature*, 435(7044):937–939, 2005. doi: 10.1038/nature03696.
- Lay, T., Ammon, C. J., Kanamori, H., Koper, K. D., Sufri, O., and Hutko, A. R. Teleseismic inversion for rupture process of the 27 February 2010 Chile (Mw 8.8) earthquake. *Geophysical Research Letters*, 37(13), 2010. doi: 10.1029/2010GL043379.
- Le Béon, M., Klinger, Y., Mériaux, A. S., Al-Qaryouti, M., Finkel, R. C., Mayyas, O., and Tapponnier, P. Quaternary morphotectonic mapping of the Wadi Araba and implications for the tectonic activity of the southern Dead Sea fault. *Tectonics*, 31(5):1–25, 2012. doi: 10.1029/2012TC003112.
- Lefevre, M. *Segmentation des grands décrochements, du cycle sismique à la déformation long terme, exemple de la faille du Levant*. PhD Thesis, Université Paris Diderot, 2018.
- Lefevre, M., Klinger, Y., Al-Qaryouti, M., Le Béon, M., and Moumani, K. Slip deficit and temporal clustering along the Dead Sea fault from paleoseismological investigations. *Sci. Rep.*, 8(1):1–9, 2018. doi: 10.1038/s41598-018-22627-9.
- Li, X., Jónsson, S., and Cao, Y. Interseismic deformation from Sentinel-1 burst-overlap interferometry: Application to the southern Dead Sea fault. *Geophys. Res. Lett.*, 48: e2021GL093481, 2021. doi: 10.1029/2021GL093481.
- Madariaga, R. High-frequency radiation from crack (stress drop) models of earthquake faulting. *Geophys. J. Int.*, 51(3):625–651, 1977. doi: 10.1111/j.1365-246X.1977.tb04211.x.

- Meier, M. A., Ampuero, J. P., and Heaton, T. H. The hidden simplicity of subduction megathrust earthquakes. *Science*, 357(6357): 1277–1281, 2017. doi: 10.1126/science.aan5643.
- Meng, L., Ampuero, J.-P., Sladen, A., and Rendon, H. High-resolution backprojection at regional distance: Application to the Haiti M 7.0 earthquake and comparisons with finite source studies. *J. Geophys. Res. Solid Earth*, 117(B4):n/a–n/a, apr 2012. doi: 10.1029/2011JB008702.
- Meng, L., Zhang, A., and Yagi, Y. Improving back projection imaging with a novel physics-based aftershock calibration approach: A case study of the 2015 Gorkha earthquake. *Geophys. Res. Lett.*, 43(2):628–636, 2016. doi: 10.1002/2015GL067034.
- Minson, S. E., Simons, M., and Beck, J. L. Bayesian inversion for finite fault earthquake source models I-theory and algorithm. *Geophys. J. Int.*, 194(3):1701–1726, 2013. doi: 10.1093/gji/ggt180.
- Moral, P. D., Doucet, A., and Jasra, A. Sequential Monte Carlo samplers. *J.R. Statist. Soc. B.*, 68(3):411–436, 2006.
- Mustać, M., Hejrani, B., Tkalčić, H., Kim, S., Lee, S. J., and Cho, C. S. Large isotropic component in the source mechanism of the 2013 democratic people's Republic of Korea nuclear test revealed via a hierarchical Bayesian inversion. *Bull. Seismol. Soc. Am.*, 110(1): 166–177, 2020. doi: 10.1785/0120190062.
- Okuwaki, R. and Yagi, Y. Role of geometric barriers in irregular-rupture evolution during the 2008 Wenchuan earthquake. *Geophys. J. Int.*, 212(3):1657–1664, 2018. doi: 10.1093/gji/ggx502.
- Palo, M., Tilmann, F., Krueger, F., Ehlert, L., and Lange, D. High-frequency seismic radiation from Maule earthquake (M w 8.8, 2010 February 27) inferred from high-resolution backprojection analysis. *Geophys. J. Int.*, 199(2):1058–1077, 2014. doi: 10.1093/gji/ggu311.
- Pinar, A. and Türkelli, N. Source inversion of the 1993 and 1995 Gulf of Aqaba earthquakes. *Tectonophysics*, 283(1-4):279–288, 1997. doi: 10.1016/S0040-1951(97)00070-X.
- Ribot, M., Klinger, Y., Jónsson, S., Avsar, U., Pons-Branchu, E., Matrau, R., and Mallon, F. L. Active Faults' Geometry in the Gulf of Aqaba, Southern Dead Sea Fault, Illuminated by Multi-beam Bathymetric Data. *Tectonics*, 40(4):1–13, 2021. doi: 10.1029/2020TC006443.
- Rössler, D., Krueger, F., Ohrnberger, M., and Ehlert, L. Rapid characterisation of large earthquakes by multiple seismic broadband arrays. *Nat. Hazards Earth Syst. Sci.*, 10(4):923–932, 2010. doi: 10.5194/nhess-10-923-2010.
- Schimmel, M. and Paulssen, H. Noise reduction and detection of weak, coherent signals through phase-weighted stacks. *Geophys. J. Int.*, 130(2):497–505, 1997. doi: 10.1111/j.1365-246X.1997.tb05664.x.
- Schwarz, G. Estimating the Dimension of a Model. *The Annals of Statistics*, 6(2):461 – 464, 1978. doi: 10.1214/aos/1176344136.
- Shamir, G., Baer, G., and Hofstetter, A. Three-dimensional elastic earthquake modelling based on integrated seismological and InSAR data: the M w = 7.2 Nuweiba earthquake, gulf of Elat/Aqaba 1995 November. *Geophys. J. Int.*, 154(3):731–744, sep 2003. doi: 10.1046/j.1365-246X.2003.01978.x.
- Shi, X., Wang, Y., Liu-Zeng, J., Weldon, R., Wei, S., Wang, T., and Sieh, K. How complex is the 2016 Mw 7.8 Kaikoura earthquake, South Island, New Zealand? *Sci. Bull.*, 62(5):309–311, 2017. doi: 10.1016/j.scib.2017.01.033.
- Spudich, P. and Frazer, L. N. Use of ray theory to calculate high-frequency radiation from earthquake sources having spatially variable rupture velocity and stress drop. *Bulletin of the Seismological Society of America*, 74(6):2061–2082, 12 1984. doi: 10.1785/BSSA0740062061.
- Steinberg, A. braunfuss/Palantiri: v0.8 (v0.8), 2021. 10.5281/zenodo.4465171.
- Steinberg, A., Sudhaus, H., and Krüger, F. Using teleseismic backprojection and InSAR to obtain segmentation information for large earthquakes: a case study of the 2016 M w 6.6 Muji earthquake. *Geophys. J. Int.*, 232(3):1482–1502, 2022. doi: 10.1093/gji/ggac392.
- Steinhaus, H. Sur la division des corp materiels en parties. *Bull. Acad. Polon. Sci*, 1(804):801, 1956.
- Sudhaus, H. and Jónsson, S. Improved source modelling through combined use of InSAR and GPS under consideration of correlated data errors: application to the June 2000 Kleifarvatn earthquake, Iceland. *Geophys. J. Int.*, 176(2):389–404, feb 2009. doi: 10.1111/j.1365-246X.2008.03989.x.
- Tinti, E., Fukuyama, E., Piatanesi, A., and Cocco, M. A kinematic source-time function compatible with earthquake dynamics. *Bull. Seismol. Soc. Am.*, 95(4):1211–1223, 2005. doi: 10.1785/0120040177.
- Vasyura-Bathke, H., Dettmer, J., Steinberg, A., Heimann, S., Isken, M., Zielke, O., Mai, P. M., Sudhaus, H., and Jónsson, S. BEAT - Bayesian Earthquake Analysis Tool. *GFZ Data Services*, v.1.0, 2019.
- Vasyura-Bathke, H., Dettmer, J., Steinberg, A., Heimann, S., Isken, M. P., Zielke, O., Mai, P. M., Sudhaus, H., and Jónsson, S. The Bayesian Earthquake Analysis Tool. *Seismol. Res. Lett.*, 91(2A): 1003–1018, jan 2020. doi: 10.1785/0220190075.
- Vasyura-Bathke, H., Dettmer, J., Dutta, R., Mai, P. M., and Jónsson, S. Accounting for theory errors with empirical Bayesian noise models in nonlinear centroid moment tensor estimation. *Geophys. J. Int.*, jan 2021. doi: 10.1093/gji/ggab034.
- Vasyura-Bathke, H., Steinberg, A., Krüger, F., Guangcai, F., Mai, P. M., and Jónsson, S. InSAR derived surface displacement maps of the 1995 Gulf of Aqaba earthquake [Data set], 2024. 10.5281/zenodo.10462416.
- Viltres, R., Jónsson, S., Alothman, A., Liu, S., Leroy, S., Masson, F., Doubre, C., and Reilinger, R. Present-day motion of the Arabian Plate. *Tectonics*, 41:e2021TC00713, 2022. doi: 10.1029/2021TC007013.
- Virtanen, P., Gommers, R., Oliphant, T. E., Haberland, M., Reddy, T., Cournapeau, D., Burovski, E., Peterson, P., Weckesser, W., Bright, J., van der Walt, S. J., Brett, M., Wilson, J., Millman, K. J., Mayorov, N., Nelson, A. R. J., Jones, E., Kern, R., Larson, E., Carey, C. J., Polat, b., Feng, Y., Moore, E. W., VanderPlas, J., Laxalde, D., Perktold, J., Cimrman, R., Henriksen, I., Quintero, E. A., Harris, C. R., Archibald, A. M., Ribeiro, A. H., Pedregosa, F., van Mulbregt, P., and SciPy 1.0 Contributors. SciPy 1.0: Fundamental Algorithms for Scientific Computing in Python. *Nature Methods*, 17:261–272, 2020. doi: 10.1038/s41592-019-0686-2.
- Wald, D. J. and Allen, T. I. Topographic slope as a proxy for seismic site conditions and amplification. *Bulletin of the Seismological Society of America*, 97(5):1379–1395, 2007. doi: 10.1785/0120060267.
- Wang, D., Kawakatsu, H., Mori, J., Ali, B., Ren, Z., and Shen, X. Back-projection analyses from four regional arrays for rupture over a curved dipping fault: The Mw 7.7 24 September 2013 Pakistan earthquake. *J. Geophys. Res. Solid Earth*, 121(3):1948–1961, 2016. doi: 10.1002/2015JB012168.
- Wang, R. A simple orthonormalization method for stable and efficient computation of Green's functions. *Bull. Seismol. Soc. Am.*, 89(3):733–741, 1999. doi: 10.1785/BSSA0890030733.
- Wang, R., Lorenzo-Martín, F., and Roth, F. PSGRN / PSCMP — a new code for calculating co- and post-seismic deformation, geoid and gravity changes based on the viscoelastic-gravitational displacement theory. *Comput. Geosci.*, 32(4):527–541, 2006. doi:

10.1016/j.cageo.2005.08.006.

Wang, R., Heimann, S., Zhang, Y., Wang, H., and Dahm, T. Complete synthetic seismograms based on a spherical self-gravitating Earth model with an atmosphere – ocean – mantle – core structure. *Geophys. J. Int.*, 210:1739–1764, 2017. doi: 10.1093/gji/ggx259.

Wegmüller, U. SAR Processing, Interferometry, Differential Interferometry and Geocoding Software, 1998. presented at EU-SAR'98, 25-27 May.

Wesnousky, S. Predicting the endpoints of earthquake rupture. *Nature*, 444(7117):358–360, 2006. doi: 10.1038/nature05275.

Wessel, P., Smith, W. H. F., Scharroo, R., Luis, J., and Wobbe, F. Generic Mapping Tools: Improved Version Released. *EOS Trans. AGU*, 94(45):409–410, 2013. doi: 10.1002/2013EO450001.

The article *Discontinuous transtensional rupture during the Mw 7.2 1995 Gulf of Aqaba earthquake* © 2024 by Hannes Vasyura-Bathke is licensed under CC BY 4.0.